Featured in Physics

Simulating Models of Challenging Correlated Molecules and Materials on the Sycamore Quantum Processor

Ruslan N. Tazhigulov,[1] Shi-Ning Sun,[2] Reza Haghshenas,[1] Huanchen Zhai,[1] Adrian T.K. Tan,[2] Nicholas C. Rubin,[3] Ryan Babbush,[3] Austin J. Minnich,[2] and Garnet Kin-Lic Chan[1,*]

[1] *Division of Chemistry and Chemical Engineering, California Institute of Technology, Pasadena, California 91125, USA*

[2] *Division of Engineering and Applied Science, California Institute of Technology, Pasadena, California 91125, USA*

[3] *Google Quantum AI, 340 Main Street, Venice, California 90291, USA*

(Received 10 July 2022; revised 7 September 2022; accepted 11 October 2022; published 14 November 2022)

Simulating complex molecules and materials is an anticipated application of quantum devices. With the emergence of hardware designed to target strong quantum advantage in artificial tasks, we examine how the same hardware behaves in modeling physical problems of correlated electronic structure. We simulate static and dynamical electronic structure on a superconducting quantum processor derived from Google's Sycamore architecture for two representative correlated electron problems: the nitrogenase iron-sulfur molecular clusters and α-ruthenium trichloride, a proximate spin-liquid material. To do so, we simplify the electronic structure into low-energy spin models that fit on the device. With extensive error mitigation and assistance from classical recompilation and simulated data, we achieve quantitatively meaningful results deploying about one fifth of the gate resources used in artificial quantum advantage experiments on a similar architecture. This increases to over half of the gate resources when choosing a model that suits the hardware. Our work serves to convert artificial measures of quantum advantage into a physically relevant setting.

DOI: 10.1103/PRXQuantum.3.040318

I. INTRODUCTION

There has been much interest in simulating problems of chemistry and materials science on quantum computers [1,2]. This is not least because the first claims of potential quantum "advantage" in a number of tasks have appeared [3–5]. Such simulations have deployed an impressive level of quantum resources; the random-circuit-advantage experiments on the Sycamore processor used more than 50 qubits and approximately 500 two-qubit gates. However, the common feature of recent attempts to reach quantum advantage is their artificial nature. In particular, the experiments propose a special selection of tasks and metrics designed to facilitate large quantum advantage on current hardware. For example, Ref. [3] involved distinguishing a theoretical signal of 1 from 0, but a noisy experimental result of 0.002 was already been sufficient to claim success at the time due to the comparative complexity of the chosen classical algorithm to obtain the same result. The extent to which success in such a metric is transferable to generally accepted criteria for successfully simulating actual chemical and materials problems is unclear.

In this work, we study the simulation of two "realistic" (if still highly simplified) problems of strongly correlated molecular and materials electronic structure on a state-of-the-art superconducting quantum processor. Aside from the necessary simplifications, neither the systems nor the observables studied are chosen to favor the demonstration of advantage on the experimental hardware. The current work thus attempts to report on the ability of current quantum devices to tackle problems of real-world interest without careful preselection. In particular, we examine the relation between the deployable quantum resources to achieve artificial quantum advantage metrics and those that can be used in successful electronic structure simulations.

The first problem we consider is the low-energy electronic structure of the iron-sulfur clusters of nitrogenase, including the Fe-Mo cofactor, critical components of the natural nitrogen cycle. The second is the electronic structure of α-$RuCl_3$, a candidate material for realizing

*gkc1000@gmail.com

Published by the American Physical Society under the terms of the Creative Commons Attribution 4.0 International license. Further distribution of this work must maintain attribution to the author(s) and the published article's title, journal citation, and DOI.

spin-liquid physics. Both are strongly correlated electron structure problems that contain challenging features for quantitative heuristic quantum chemistry approximations. Although for practical reasons we need to reduce the electronic structure into low-energy spin models, the range, nature, and topology of the interactions provide some elements of real-world complexity that can be absent from more specially chosen simulation problems. We target finite-temperature static and dynamical properties representative of accessible physical chemistry measurements and study both systems using the Weber superconducting qubit processor derived from Google's Sycamore architecture, using the finite-temperature version of quantum imaginary time evolution with global classical recompilation of the circuits [6,7]. To obtain meaningful data, many types of error mitigation are necessary; thus we discuss the impact of different protocols. Our results illustrate to what extent current superconducting quantum processors can be used to simulate real-world chemical and materials problems.

II. RESULTS

A. Overview of systems

1. Fe-S *clusters and nitrogenase*

Nitrogenases are enzymes that convert atmospheric dinitrogen into ammonia. The process involves the coordinated transfer of multiple electrons and protons to dinitrogen and utilizes multiple metalloclusters found in the nitrogenase enzyme: the [4Fe-4S] Fe-cluster, the [8Fe-7S] P cluster, and the [7Fe-1Mo-9S] Fe-Mo cofactor (the latter can also be found with other metals replacing molybdenum) [8]. The electronic structure of the Fe-S clusters remains incompletely understood; theoretical calculations on the Fe and P clusters have unveiled a large number of low-lying spin states [9,10], the role of which in the electron-transfer process is unclear. In the case of the Fe-Mo cofactor, the oxidation and spin states of the ions are unresolved.

The simplest electronic models of these compounds involve the Fe and S valence orbitals, with over 100 spin orbitals in the case of the Fe-Mo cofactor, too large for current quantum devices [11]. However, both theoretical and spectroscopic studies indicate that the electron-hole-like excitations mostly lie at higher energies than a manifold of low-energy spin-coupled states. Thus the low-lying electronic spectrum can be captured using a variety of spin models, which are commonly used to interpret the electronic structure [9,12,13] as well as to model measured quantities, such as the magnetic susceptibility and heat capacity [14,15]. In the most commonly studied Fe-S models, the metals occupy vertices and the S bridges form the edges, with the latter enforcing antiferromagnetic interactions parametrized by the exchange coupling J [9,12]. The three-dimensional models and the two-dimensional pattern of the spin couplings are shown in Fig. 1. Although the metal ions have large total spin (e.g., $S = 2, S = 5/2$), we can further simplify (reducing the quantum resources) by representing each metal by a $S = 1/2$ spin, retaining only the topology of the spin-spin couplings, and with an isotropic Heisenberg exchange interaction between each spin pair. Although the spectrum is changed by this reduction, it retains similar features in the lowest few states, e.g., the total spin value and degeneracy, as discussed in Appendix A. The simplified Hamiltonian can thus be written as

$$\hat{H} = \sum_{ij} J_{ij} S_i S_j , \tag{1}$$

where S_i and S_j are $S = 1/2$ operators and $\langle ij \rangle$ denotes each of the bonds in Fig. 1. We note that other instances of Heisenberg models have been simulated on quantum devices (see, e.g., Refs. [16,17]) but the interesting properties of the FeS clusters relate to the specific topology and magnitudes of the spin couplings.

The magnetic model parameters in the FeS clusters are usually derived through fitting to experimental data or through *ab initio* calculations [9,12]. In the Heisenberg model, one parameter can be set as the scale of energy (J), while the antiferromagnetic nature of the interaction induced by the Fe-S-Fe bridges fixes the sign of the couplings to be positive. In the case of [4Fe-4S], we use only two different J_{ij}, namely $J = 1$ and $J' = 1.17J$, as previously determined to characterize the all-ferric cubane [18] [J' couples (1–2) and (3–4), while J couples the other pairs, as shown in Fig. 1(b)]. Deriving accurate exchange couplings in the P cluster and the Fe-Mo cofactor is more challenging; thus, noting the modest variation in J_{ij} in [4Fe-4S], we use a single J for all couplings in the P cluster and the Fe-Mo cofactor (all J positive). With this simplification, the P cluster and the Fe-Mo cofactor have the same spin Hamiltonian. (Note that the units chosen for energy define an inverse energy unit for time; all times will hence be assumed to be in such units.)

2. Ruthenium trichloride, α*-*$RuCl_3$

Ruthenium trichloride is a transition-metal material of interest as a "proximate" spin liquid [19]. Similarly to in the Fe-S clusters, the low-energy excitations are spin excitations. In particular, the edge-sharing octahedral coordination around the Ru(III) ions (see Fig. 1), together with the spin-orbit coupling, leads to a low-energy Hamiltonian that approximates the exactly solvable Kitaev model in the spin-liquid regime. However, the degree of similarity to the Kitaev model, as well as the interpretation of spectroscopic and thermal measurements in terms of modifications to the Kitaev model, is much debated.

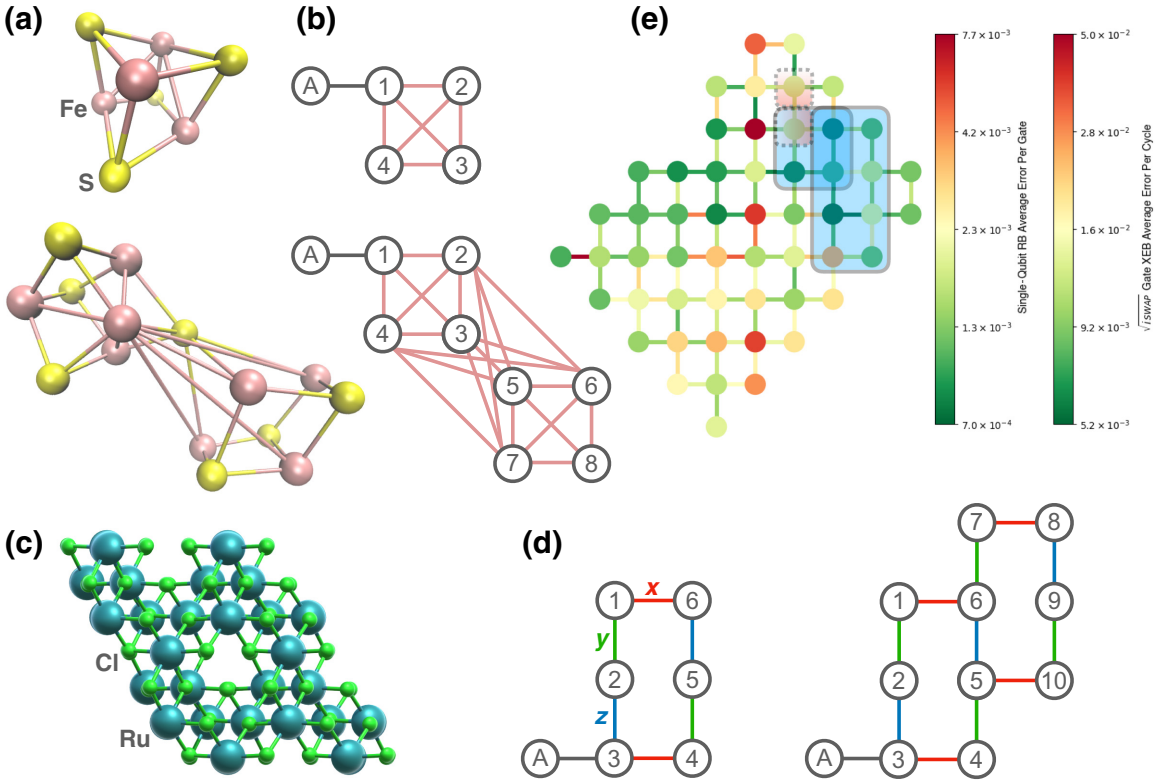

FIG. 1. (a) The molecular structures of the [4Fe-4S] and [8Fe-7S] P clusters. (b) The topology of the four-site and eight-site Heisenberg spin models of the (top) [4Fe-4S] and (bottom) [8Fe-7S] P clusters. (c) The crystal structure of α-$RuCl_3$: trigonal space group $P3_112$. (d) The topology of the six-site and ten-site Kitaev-Heisenberg spin models of α-$RuCl_3$. The adjacent ancilla qubits are indicated as "A." (e) Illustrative examples of qubit patches (blue) used for simulations of four-site and eight-site models. The ancilla qubits (dotted boxes) are shown in red. The color scheme of the qubits and connectivities represents the "single-qubit randomized benchmarking (RB) average error per gate" and "two-qubit $\sqrt{\text{iSWAP}}$ gate cross-entropy benchmarking (XEB) average error per cycle," respectively.

Much work has been devoted to deriving and parametrizing low-energy Hamiltonians for α-$RuCl_3$ [20]. The simplest family of Hamiltonians are the Kitaev-Heisenberg models, which take the form

$$\hat{H}_{\text{KH}} = J \sum_{\langle i,j \rangle} S_i S_j + K_\gamma \sum_{\langle i,j \rangle^\gamma} S_i^\gamma S_j^\gamma, \tag{2}$$

where $\gamma = X, Y, Z$. We also use a parametrization in the literature from Refs. [20–22], where the above form is augmented by additional couplings:

$$\begin{aligned}\hat{H}_{\text{KH}} = {} & J \sum_{\langle i,j \rangle} S_i S_j + K_\gamma \sum_{\langle i,j \rangle^\gamma} S_i^\gamma S_j^\gamma \\ & + \Gamma \sum_{\langle i,j \rangle} (S_i^\alpha S_j^\beta + S_i^\beta S_j^\alpha) \\ & + \Gamma' \sum_{\langle i,j \rangle} \sum_{\alpha \neq \gamma} (S_i^\gamma S_j^\alpha + S_i^\alpha S_j^\gamma),\end{aligned} \tag{3}$$

where γ $(\alpha, \beta) = X, Y, Z$, and α and β take indices different from γ. Specifically, we use the parameters: $J = -1.53$, $K = K_\gamma = -24.4$, $\Gamma = 5.25$, and $\Gamma' = -0.95$. The Kitaev point, which is exactly solvable, corresponds to taking only the K_γ term in the above models. It is argued that in the parameter regime of α-$RuCl_3$, both the excitations and heat capacity show echoes of the two kinds of Majorana fermions that exist at the exactly solvable point [23,24].

B. Implementation

1. Formal algorithm

We simulate the finite-temperature energies and dynamical correlation functions of the systems. The quantum imaginary time evolution (QITE) algorithm is used to prepare a sample of the finite-temperature state $\rho = e^{-\beta H}/\text{Tr}(e^{-\beta H})$. The basic idea in QITE is to prepare normalized imaginary time-evolved states $e^{-\beta H/2}|\Psi_i(0)\rangle = c_i(\beta) U_i(\beta/2)|\Psi_i(0)\rangle$ on the quantum device. Here, $c_i(\beta)$ is a normalization constant tracked classically, $U_i(\beta/2)$ is the unitary determined by the QITE procedure, and $|\Psi_i(0)\rangle$ is the initial state (here, the ith computational-basis state). We are interested in the finite-temperature static and dynamical observables $\langle A \rangle_\beta = \text{Tr}[\rho A]$ and $\langle A(t) B \rangle =$

$\mathrm{Tr}[\rho A(t)B]$, computed as

$$\langle \hat{A} \rangle_\beta = \frac{\sum_i P_i A_i}{\sum_i P_i}, \tag{4}$$

where $P_i = |c_i(\beta)|^2$ and $A_i = \langle \Psi_i(\beta/2)|\hat{A}|\Psi_i(\beta/2)\rangle$. The expectation values A_i are obtained by reading out Pauli operators (static observables) or from the Hadamard test (dynamic observables).

In the original QITE procedure, the unitaries are determined at each time step from a set of linear equations constructed from measurements on the quantum device. Similarly, the normalization weights P_i are accumulated at each time step. Once the imaginary time states $|\Psi_i(\beta/2)\rangle$ are prepared, they can then be propagated in real time to yield states $|\Psi_i(\beta/2 + t)\rangle$, with the real-time propagation unitary $U(t)$ generated, e.g., by a Trotter evolution of the Hamiltonian. The schematic circuit for a dynamical simulation is shown in Fig. 1(a). In the current experiments, however, we use classical recompilation [7] to generate both the circuits $U(\beta/2)$ and $U(t)$ and the weights P_i. The details are described further below.

2. Implementation and error mitigation

Hardware and qubit selection. The simulations are run on Google's 53-qubit Weber processor based on the Sycamore architecture [3]. The Fe-S cluster simulations use up to five and nine qubits, respectively, while the α-$RuCl_3$ simulations use up to seven and 11 qubits, respectively. (In the above qubit counts, we include the one ancilla qubit used for the Hadamard test circuit.) The best-performing qubits are selected using a combination of single-qubit randomized benchmarking, two-qubit cross-entropy benchmarking, and Loschmidt-echo metrics on the hardware; an example of the embedding of the qubits onto the Weber architecture for the Fe-S clusters is shown in Fig. 1(e).

Circuit recompilation. The circuit realization of the formal QITE algorithm [including $U(\beta/2)$ and $U(t)$] using a reasonable Trotter time step (e.g., 0.1 inverse energy units) is far too deep for current quantum devices. For example, using a first-order Trotter expansion with a time step of 0.1 in the six-site Kitaev-Heisenberg model at the Kitaev point, we already exceed the two-qubit gate count used in random-circuit advantage after three units of time. Thus, to reduce the circuit depth, for each desired imaginary-time or imaginary- plus real-time point at which observables are to be measured, we define the corresponding U_i by classical recompilation. This is a variational procedure whereby the exact unitary is constructed classically and then a circuit of given depth ($\bar{U}_i$) is (classically) variationally optimized to maximize the fidelity $||U_i|\Psi_i(0)\rangle - \bar{U}_i|\Psi_i(0)\rangle||$ [7]. We note that classical optimization of the global fidelity is not a scalable procedure but it is necessary to produce the best results on quantum hardware; optimization to reproduce marginals (density matrices) could, in principle, be used if scalability was important [7]. To represent $\bar{U}_i$, we choose a brickwork circuit of the native gates [single-qubit phased XZ (PhXZ) and two-qubit $\sqrt{\mathrm{iSWAP}}^\dagger$], adjusted for systematic errors (see below) and we recompile to a

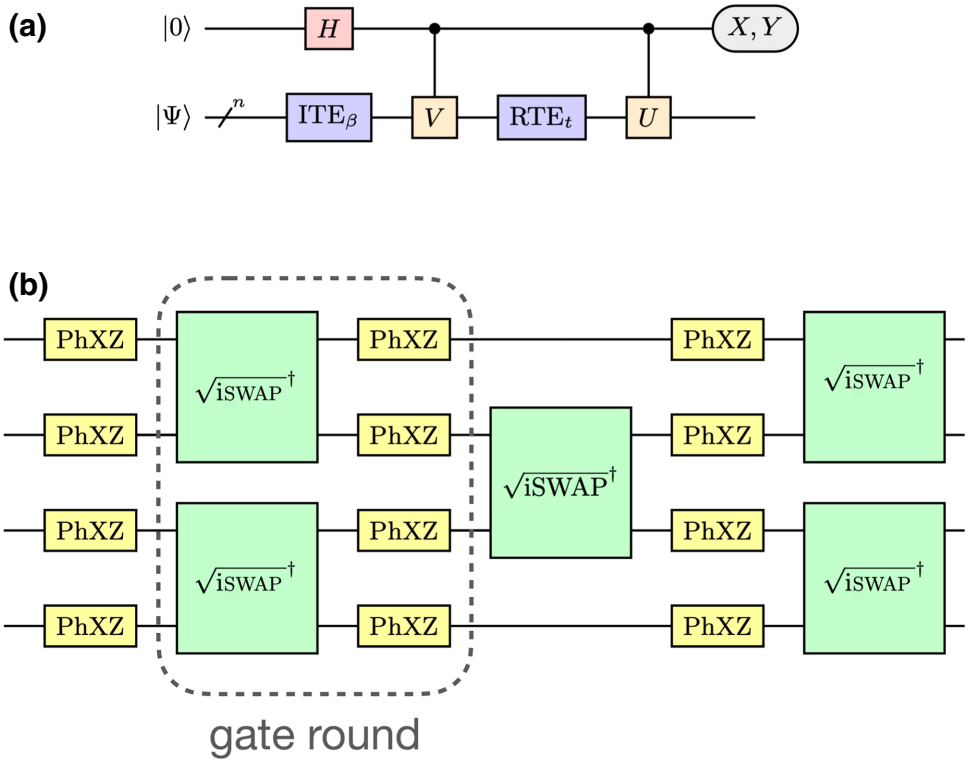

FIG. 2. (a) The quantum circuit to calculate a finite-temperature dynamic correlation function $\langle \hat{U}(t)\hat{V}\rangle_\beta$ using QITE and one ancilla qubit. Measuring X and Y on the ancilla yields the real and imaginary parts of the correlation function, respectively. The thermal average over the initial states is obtained according to Eq. (4). (b) The circuit-recompilation ansatz. Each gate round after the base PhXZ layer includes a layer of two-qubit $\sqrt{\mathrm{iSWAP}}^\dagger$ and single-qubit PhXZ gates, as shown in the box.

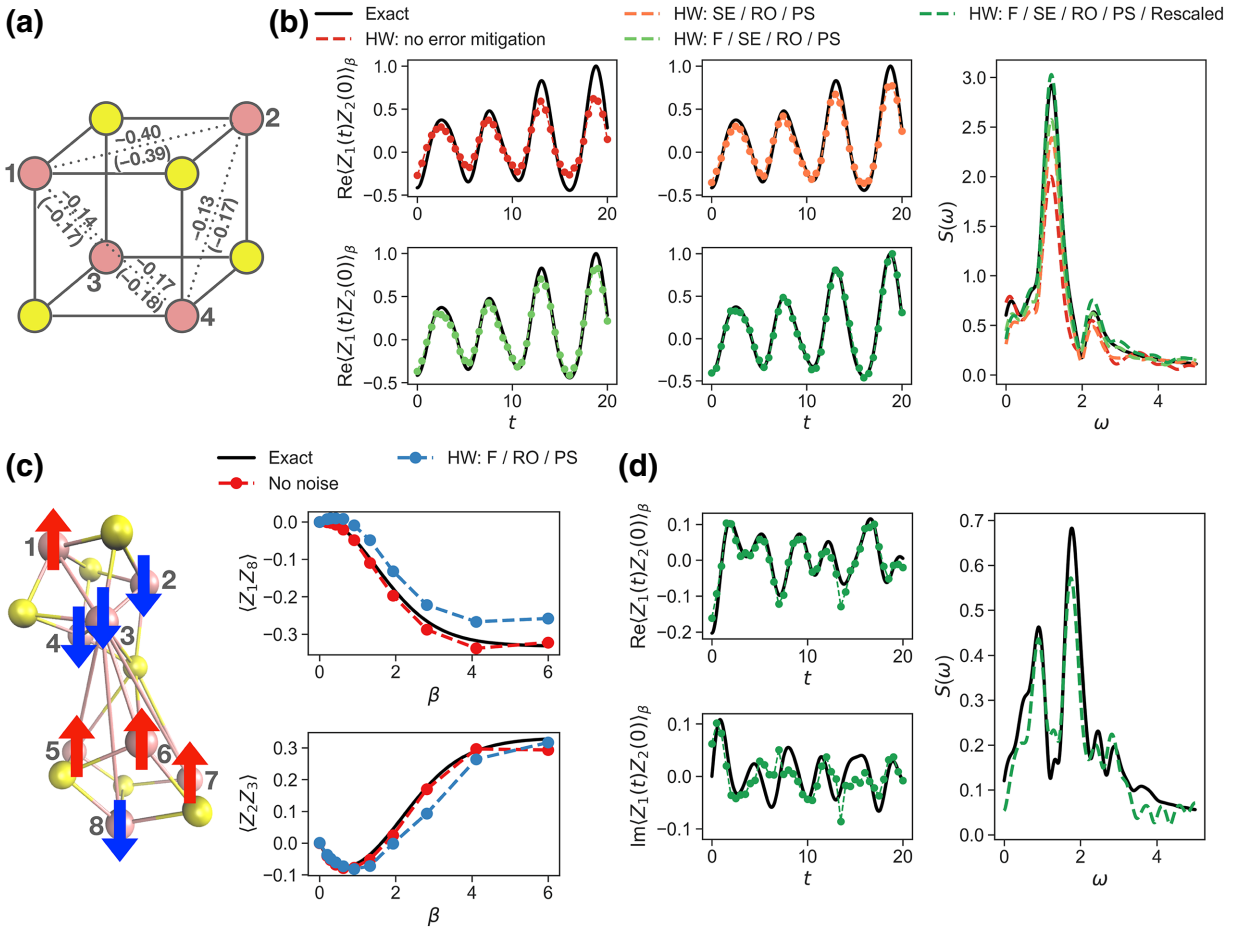

FIG. 3. (a) The finite-temperature $\langle Z_i Z_j \rangle$ ($\beta = 2$) correlation functions computed for the [4Fe-4S] model. The simulation values are in good agreement with the exact results in parentheses. (b) The finite-temperature dynamical correlation function $\langle Z_1(t)Z_2(0)\rangle_\beta$ ($\beta = 2$) and its Fourier transform for the [4Fe-4S] model. (c) The spin-coupling pattern (derived from $\langle Z_i Z_j \rangle$ correlation functions) in the P-cluster and/or Fe-Mo–cofactor model and the simulated finite-temperature $\langle Z_1 Z_8 \rangle$ and $\langle Z_2 Z_3 \rangle$ for the model, showing the correct magnetic coupling pattern in the low-temperature regime. The deviation between the exact and no-noise results shows the effects of recompilation. (d) The real and imaginary parts of the finite-temperature dynamical correlation function $\langle Z_1(t)Z_2(0)\rangle_\beta$ ($\beta = 1$) and its Fourier transform for the P-cluster and/or Fe-Mo–cofactor model. Error-mitigation acronyms: SE, spin echoes; F, Floquet calibration; RO, readout-error mitigation; PS, postselection; HW, hardware.

fidelity of $> 90\%$ in classical noiseless emulations [see Fig. 2(b)].

Postselection. The Fe-S clusters and simplified α-$RuCl_3$ Hamiltonians possess Z_2 symmetry. We use this to perform postselection as discussed in Ref. [7].

Floquet calibration. As discussed in Refs. [25,26], one can calibrate an "excitation-number"-conserving gate in terms of five angles: θ, ϕ, ζ, γ, and χ. The ideal $\sqrt{\text{iSWAP}}^\dagger$ gate should have $\theta = \pi/4$, with all other angles being zero, but in practice this is not the case. We perform "Floquet" calibration [25,26] before each experiment to calibrate the actual angles for each run. The modified $\sqrt{\text{iSWAP}}^\dagger$ gate is then used in the classical recompilation procedure to obtain the most faithful compressed circuit.

It is important to note that this calibration is only performed on isolated $\sqrt{\text{iSWAP}}^\dagger$ gates. However, due to the specifics of the hardware, the presence of PhXZ gates ("microwave" gates) can lead to additional errors in the two-qubit gates that are not accounted for in the calibration.

Dynamical decoupling. In the schematic shown in Fig. 2(a) for dynamical observables, the ancilla qubit in the Hadamard test is idle for large parts and can decohere. To mitigate this effect, we employ a dynamical decoupling sequence [27,28] consisting of inserting identities generated by XX and YY gates on the ancilla.

Rescaling. To improve the data, we perform postprocessing, rescaling all dynamical correlation functions. To do so, we perform a classical noiseless simulation using

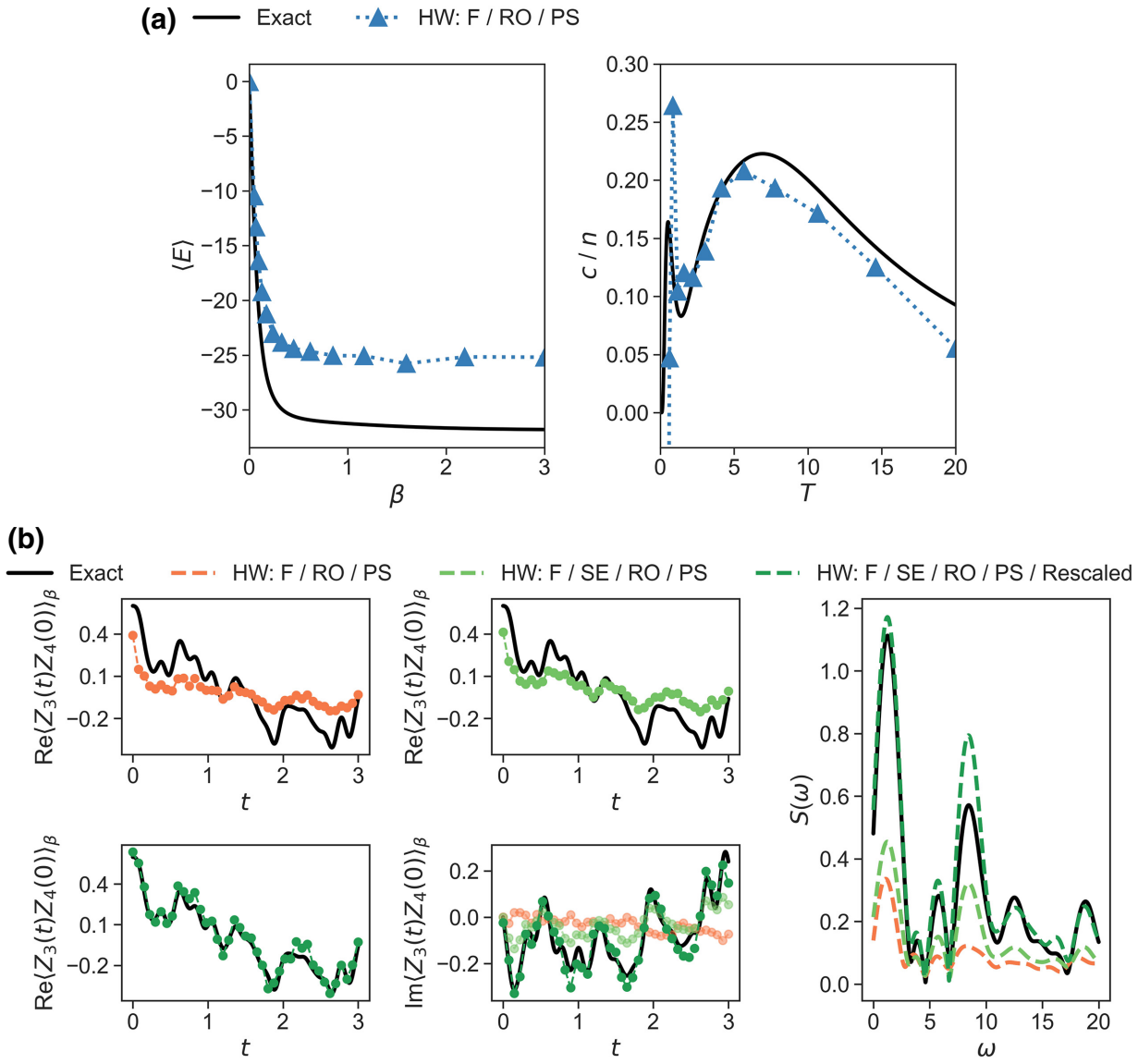

FIG. 4. (a) The thermal energy $\langle E\rangle$ and heat capacity ($c/n = \frac{1}{n}\partial\langle E\rangle/\partial T$) for the α-$RuCl_3$ six-site model ($n = 6$). The two-peak structure is indicative of the proximate spin-liquid character [29–31]. (b) The dynamical correlation function $\langle Z_3(t)Z_4(0)\rangle_\beta$ and its transform $S(\omega)$ at $\beta = 1$ for the α-$RuCl_3$ six-site model. The three plots for the real part show the successive improvement obtained by standard error mitigation (Floquet, readout error, postselection, orange); the introduction of spin echoes (light green); and rescaling (dark green). The same is seen in the plots for the imaginary part and for $S(\omega)$, where the results successively including these three classes of techniques are superposed. Error-mitigation acronyms: SE, spin echoes; F, Floquet calibration; RO, readout-error mitigation; PS, postselection; HW, hardware.

a modified Hamiltonian $\hat{H}'$ containing only commuting terms on pairs of qubits. For example, for the hexagonal model shown in Fig. 1(d), we use only the Hamiltonian terms on (1–2), (3–4), and (5–6). The commuting form of $\hat{H}'$ means that the exact classical simulation can be performed easily. We then perform the same simulation on the quantum device, generating the circuit by recompilation with the same ansatz as for the full Hamiltonian and including all the error-mitigation techniques described above. It is important to note that even though $\hat{H}'$ contains only commuting terms, the ansatz used for the quantum device does not have this simplifying commuting structure—e.g., in Fig. 1(b), the $\sqrt{\text{iSWAP}}^\dagger$ gates couple all the qubits—thus the quantum simulation of $\hat{H}'$ samples similar noise to that of $\hat{H}$. For each time point t (in imaginary and in real time), we then define a rescaling factor

$$f(t) = \frac{\langle A\rangle_t^{\text{ideal}}(\hat{H}')}{\langle A\rangle_t^{\text{hardware}}(\hat{H}')}, \tag{5}$$

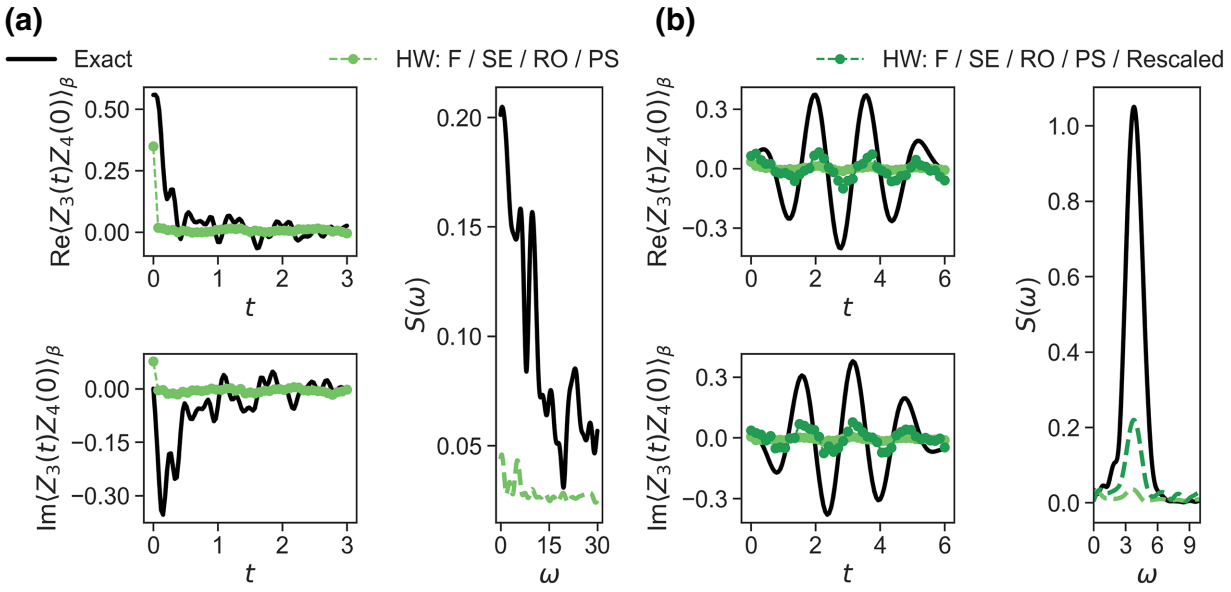

FIG. 5. (a) The dynamical correlation function $\langle Z_3(t)Z_4(0)\rangle_\beta$ and its transform $S(\omega)$ at $\beta = 1$ for the α-$RuCl_3$ ten-site model. Even after all error-mitigation strategies (light green), the data in this case are too degraded to rescale. (b) The dynamical correlation function $\langle Z_3(t)Z_4(0)\rangle_\beta$ and its transform $S(\omega)$ at $\beta = 1$ for strongly anisotropic Kitaev-Heisenberg model parameters: $J = 0.4$, $K_x = -8$, and $K_y = K_z = \frac{K_x}{6}$. Reasonable frequencies are obtained after rescaling (dark green). Error-mitigation acronyms: SE, spin echoes; F, Floquet calibration; RO, readout-error mitigation; PS, postselection; HW, hardware.

where $\langle A\rangle_t^{\text{ideal}}(\hat{H}')$ is obtained using classical noiseless emulation and $\langle A\rangle_t^{hw}(\hat{H}')$ is obtained from the hardware. $f(t)$ is then used to rescale the dynamical correlation functions of the real Hamiltonian.

C. Simulations

1. Fe-S *clusters*

Figure 3 shows simulation results on the Fe-S clusters. Despite the simplifications of the model (e.g., to $S = 1/2$), the static Z_iZ_j correlation functions at the lowest temperature ($\beta = 2$) for the [4Fe-4S] and P and/or Fe-Mo–cofactor clusters reflect the known ground-state pairing patterns of the spins in the true [4Fe-4S] and P clusters [Figs. 3(a) and 3(c)]. The largest error in the correlation functions is approximately 22% in the P and/or Fe-Mo–cofactor cluster. The majority of this error is from the hardware rather than the classical recompilation; the error from classical recompilation can be seen in the difference between the red and black lines in Fig. 3(c).

Figure 3(b) shows the dynamical correlation functions and the effects of the different error-mitigation strategies. The total circuit complexity for the [4Fe-4S] cluster dynamical correlation function is 22 two-qubit gates after circuit recompilation of the imaginary-time evolution and real-time evolution blocks and decomposition of the controlled gates [Fig. 2(a)] into $\sqrt{\text{iSWAP}}^\dagger$ gates; as discussed, the recompilation provides nearly exact results in the classical noiseless emulator, indistinguishable from the exact results on the plot. Even without error mitigation, the dynamics displays the right frequencies [Fig. 3(b)] but the amplitudes of the peaks are reduced. (We obtain some insight into the hardware performance by modeling the unmitigated results using a depolarizing noise channel in Appendix B.) The highest-amplitude peak in the spectrum ($\omega = 1.17$) represents a transition between the second excited state and ground state. Error mitigation reduces the error in the peak height by about 50%, while postprocessing (rescaling) creates an almost perfect amplitude.

The total recompiled circuit complexity for the P and/or Fe-Mo–cofactor cluster dynamical correlation functions is 82 two-qubit gates. The larger circuit complexity is reflected in the somewhat lower quality of the dynamical correlation functions. Up to frequency $\omega = 3$ (units of energy), there are seven identifiable peaks in the spectrum. Encouragingly, the hardware results even before rescaling capture the correct frequency of most of these peaks; however, the amplitudes are severely degraded: the largest-amplitude peak is only about 40% of the expected height. Postprocessing of the data (rescaling as well as shifting to satisfy the imaginary part to zero mean) significantly improves the results, although the largest-amplitude peak still has an amplitude error of 20%.

2. *Ruthenium trichloride, α-$RuCl_3$*

Figure 4 shows simulations for six-site (seven-qubit) and ten-site (11-qubit) models of α-$RuCl_3$. Including the

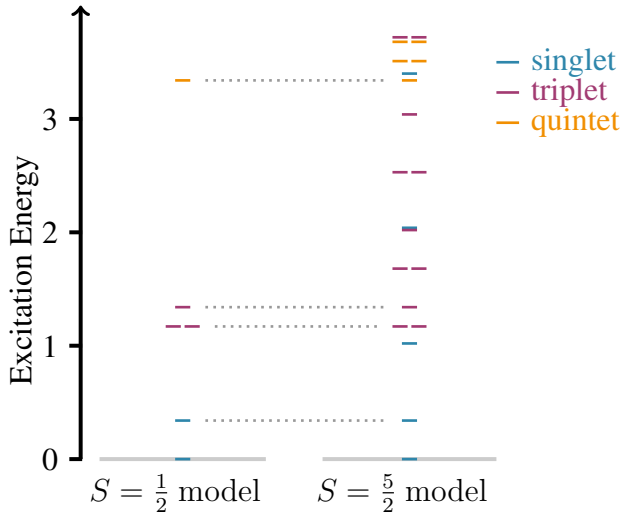

FIG. 6. The spectra of the $S = 1/2$ and $S = 5/2$ Heisenberg models for the [4Fe-4S] cluster.

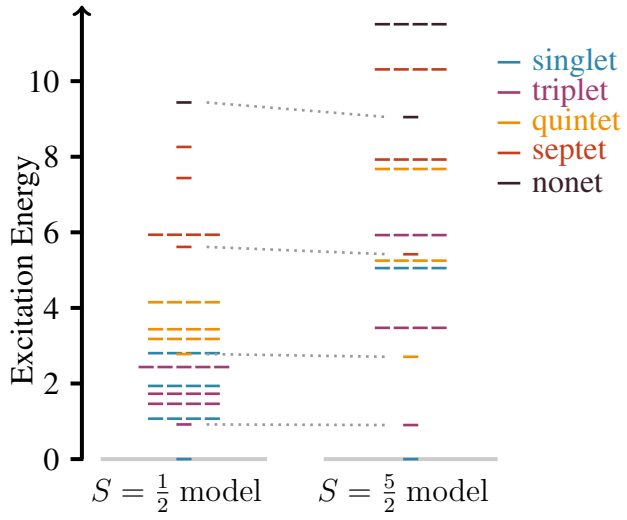

FIG. 7. The spectra of the $S = 1/2$ and $S = 5/2$ Heisenberg models for the P and/or Fe-Mo–cofactor cluster.

ancilla qubit, the latter system corresponds to the largest simulations that we perform.

We start with six-site simulations of the heat capacity, obtained by numerically differentiating the finite-temperature energies. The energy and heat capacity are shown in Fig. 4(a). One of the main features of the proximate spin-liquid behavior of α-$RuCl_3$ is a two-peak structure in the heat capacity. While the energy has a significant error at lower temperatures, the two-peak structure of the heat capacity is visible at around $T = 1$ and $T = 6 - 7$, although it is extremely noisy, as the numerical derivative amplifies the noise.

Figures 4(b) and 5(a) show the dynamical correlation functions for the α-$RuCl_3$ six- and ten-site models (64 and 310 two-qubit gates, respectively), as well as a comparison with a second anisotropic parameter set (with smaller YY and ZZ terms) in Fig. 5(b). Similarly to in the FeS clusters, the frequency structure is reasonably well preserved, with error mitigation and postprocessing restoring the amplitudes for the six-site model. However, in the ten-site α-$RuCl_3$ model, the data are too degraded to obtain any reasonable physical spectra. Figure 5(b) shows the sensitivity of the quality of simulation to the choice of model, as the more anisotropic Kitaev-Heisenberg simulations are of significantly higher quality.

III. DISCUSSION AND CONCLUSIONS

In the current work, we discuss the quantum simulation of two representative real-world problems: the Fe-S clusters of nitrogenase, including the P cluster and the Fe-Mo cofactor, a problem of interest in correlated quantum chemistry, and the proximate spin liquid α-$RuCl_3$, a correlated material. These systems are not selected for their suitability for implementation on the Sycamore platform and for practical computation, simplification of the Hamiltonians into effective low-energy spin models is required. Some reasonable results are obtained for such simplified models of these problems. In the Fe-S clusters and the smaller α-$RuCl_3$ instance, qualitatively correct features in the spin structure, excited-state spectrum, and heat capacity can be obtained. However, to achieve this, the

TABLE I. The excitation energy levels of the $S = 1/2$ and $S = 5/2$ Heisenberg models for the [4Fe-4S] cluster. The numbers in parentheses indicate the degeneracy.

$S = 1/2$ Heisenberg model			$E_{GS} = -1.755$ (singlet)				
Singlet	0.000	0.340					
Triplet	1.170 (×2)	1.340					
Quintet	3.340						
$S = 5/2$ Heisenberg model			$E_{GS} = -20.475$ (singlet)				
Singlet	0.000	0.340	1.020	2.040	3.400		
Triplet	1.170 (×2)	1.340	1.680 (×2)	2.020	2.530 (×2)	3.040	3.720 (×2)
Quintet	3.340	3.510 (×2)	3.680 (×2)				

TABLE II. The excitation energy levels of the $S = 1/2$ and $S = 5/2$ Heisenberg models for the P and/or Fe-Mo–cofactor cluster.

$S = 1/2$ Heisenberg model			$E_{GS} = -4.186$ (singlet)	
Singlet	0.000	1.070 (×4)	1.936 (×4)	2.803 (×4)
Triplet	0.917	1.463 (×4)	1.729 (×4)	2.436 (×5)
Quintet	2.779	3.179 (×4)	3.436 (×4)	4.150 (×4)
Septet	5.614	5.936 (×4)	7.436	8.259
Nonet	9.436			
$S = 5/2$ Heisenberg model			$E_{GS} = -65.862$ (singlet)	
Singlet	0.000	5.054 (×4)	10.126 (×9)	
Triplet	0.901	3.473 (×4)	5.927 (×4)	8.518 (×12)
Quintet	2.707	5.251 (×4)	7.676 (×4)	7.941 (×6)
Septet	5.420	7.926 (×4)	10.311 (×4)	10.562 (×6)
Nonet	9.049	11.506 (×4)	13.841 (×4)	14.076 (×6)

implemented circuits need to be obtained with the help of classical recompilation and the data require significant processing, including using data from exact classical simulations of related tractable problems. Unfortunately, these steps raise questions with regard to effectively simulating more classically difficult systems.

The main limitation in the experiments is the two-qubit gate count, rather than the number of qubits. Simulations with up to 100 two-qubit gates, such as the larger Fe-S cluster simulations and the six-site α-$RuCl_3$ simulations, can be carried out with some confidence on the hardware. However, our largest simulations for α-$RuCl_3$, which use 11 qubits, 310 two-qubit gates, and 782 single-qubit gates, are not successful. However, we can obtain meaningful simulation data with these quantum resources for Hamiltonian parameters that are tuned away from the α-$RuCl_3$ regime, indicating the impact of tuning the problem for the characteristics of the hardware. The successfully deployed circuit resources are less than those used in some recent simulation experiments using a similar chip [25]. However, the discrepancy may also be understood in terms of how well the experiment matches the capabilities of the chip. For example, the simulations of the free-fermion dynamics in Ref. [25] do not require microwave gates, which helps with Floquet calibration and allows more gates to be used.

The questions of interest in realistic molecular and materials simulations are ones that require some degree of quantitative precision. Compared to the resources deployable to achieve random-circuit advantage on the same chip architecture, our representative simulation problems can use about one fifth of the qubit and gate resources. If we adjust our models to be more tuned to the hardware, it is possible to use more than half of the gate resources of quantum advantage experiments, while retaining some level of physical accuracy. This provides an understanding of the relevance of artificial quantum advantage experiments to problems of physical simulation and reflects the current status of quantum hardware and quantum simulation.

TABLE III. The ground-state energies of the Kitaev-Heisenberg models.

$S = 1/2$ six-site α-$RuCl_3$ model	$E_{GS} = -31.852$ (singlet)
$S = 1/2$ ten-site α-$RuCl_3$ model	$E_{GS} = -55.452$ (singlet)
$S = 1/2$ ten-site strongly anisotropic model	$E_{GS} = -8.325$ (×2) (singlet)

The data sheet of the Weber device can be found in Ref. [32]. The data and scripts for the density-matrix renormalization group (DMRG) simulation in Appendix A can be found in Ref. [33]. Other data that support the findings of this study are available from the corresponding author upon reasonable request. The code used to generate the numerical results presented in this paper can be made available upon reasonable request.

ACKNOWLEDGMENTS

R.N.T., R.H., and G.K.-L.C. were supported by the U.S. Department of Energy, Office of Basic Energy Sciences, under Award No. DE-SC0019374. S.-N.S., A.T.K.T., and A.J.M. were supported by the U.S. National Science Foundation (NSF) under Award No. 1839204. Additional support for R.N.T. was provided by the Dreyfus Foundation. The quantum hardware used in this work was developed by the Google Quantum AI team. Data were collected via cloud access through Google's Quantum Computing Service.

R.N.T., R.H., and G.K.-L.C. conceptualized the project. R.N.T. and S.-N.S. designed and implemented the circuits with help from R.H., while R.N.T. executed the simulations and analyzed the results. R.N.T. and G.K.-L.C. wrote the paper. All authors discussed the results and contributed to the development of the manuscript.

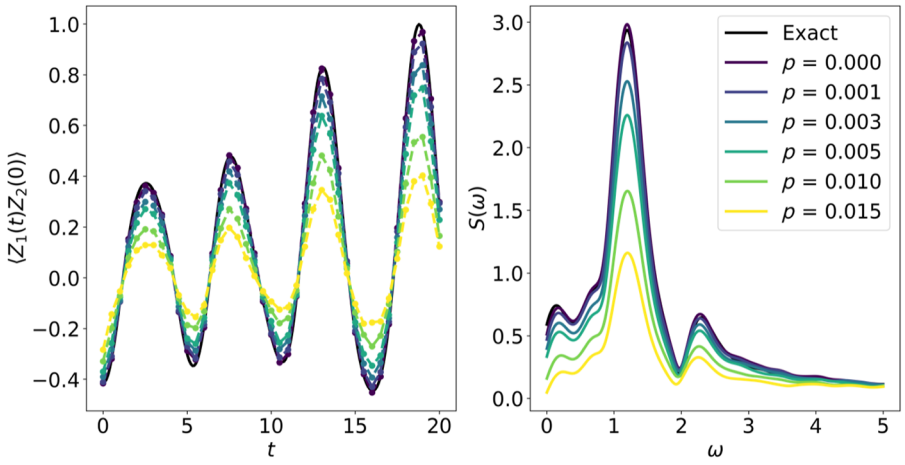

FIG. 8. Noisy emulation of the [4Fe-4S] model spectrum.

G.K.-L.C. is a part owner of QSimulate, Inc.

APPENDIX A: SPECTRUM OF $S = 5/2$ Fe-S MODELS VERSUS $S = 1/2$ Fe-S MODELS

As mentioned in the main text, the $S = 1/2$ model Fe-S spectrum has some features of the more realistic $S = 5/2$ model spectrum. This is illustrated in Figs. 6 and 7. The low-energy excitation levels are listed in Tables I and II. The data are obtained from a classical spin-adapted DMRG simulation using the open-source code BLOCK2 [34].

The ground-state energies of Kitaev-Heisenberg models are listed in Table III.

APPENDIX B: DEPOLARIZING NOISE IN THE Fe-S SIMULATION

We model depolarizing noise in classical emulation by inserting symmetric depolarizing noise after each circuit moment:

$$\rho \to (1-3p)\rho + p(X\rho X + Y\rho Y + Z\rho Z). \tag{B1}$$

The result of such a noisy emulation is shown in Fig. 8. Comparing with the data in Fig. 3(b), we see that the hardware result without error mitigation can be reproduced with a depolarizing noise value of $p = 0.005 - 0.010$.

[1] B. Bauer, S. Bravyi, M. Motta, and G. K.-L. Chan, Quantum algorithms for quantum chemistry and quantum materials science, Chem. Rev. **120**, 12685 (2020).

[2] S. McArdle, S. Endo, A. Aspuru-Guzik, S. C. Benjamin, and X. Yuan, Quantum computational chemistry, Rev. Mod. Phys. **92**, 015003 (2020).

[3] F. Arute *et al.*, Quantum supremacy using a programmable superconducting processor, Nature **574**, 505 (2019).

[4] Y. Wu *et al.*, Strong Quantum Computational Advantage Using a Superconducting Quantum Processor, Phys. Rev. Lett. **127**, 180501 (2021).

[5] H.-S. Zhong *et al.*, Quantum computational advantage using photons, Science **370**, 1460 (2020).

[6] M. Motta, C. Sun, A. T. Tan, M. J. O'Rourke, E. Ye, A. J. Minnich, F. G. Brandão, and G. K.-L. Chan, Determining eigenstates and thermal states on a quantum computer using quantum imaginary time evolution, Nat. Phys. **16**, 205 (2020).

[7] S. N. Sun, M. Motta, R. N. Tazhigulov, A. T. Tan, G. K.-L. Chan, and A. J. Minnich, Quantum Computation of Finite-Temperature Static and Dynamical Properties of Spin Systems Using Quantum Imaginary Time Evolution, PRX Quantum **2**, 010317 (2021).

[8] H. Beinert, R. H. Holm, and E. Münck, Iron-sulfur clusters: Nature's modular, multipurpose structures, Science **277**, 653 (1997).

[9] S. Sharma, K. Sivalingam, F. Neese, and G. K.-L. Chan, Low-energy spectrum of iron-sulfur clusters directly from many-particle quantum mechanics, Nat. Chem. **6**, 927 (2014).

[10] Z. Li, S. Guo, Q. Sun, and G. K.-L. Chan, Electronic landscape of the P-cluster of nitrogenase as revealed through many-electron quantum wavefunction simulations, Nat. Chem. **11**, 1026 (2019).

[11] Z. Li, J. Li, N. S. Dattani, C. Umrigar, and G. K.-L. Chan, The electronic complexity of the ground-state of the FeMo cofactor of nitrogenase as relevant to quantum simulations, J. Chem. Phys. **150**, 024302 (2019).

[12] L. Noodleman, C. Peng, D. Case, and J.-M. Mouesca, Orbital interactions, electron delocalization and spin coupling in iron-sulfur clusters, Coord. Chem. Rev. **144**, 199 (1995).

[13] K. Yamaguchi, T. Fueno, N. Ueyama, A. Nakamura, and M. Ozaki, Antiferromagnetic spin couplings between iron ions in iron-sulfur clusters. A localized picture by the spin vector model, Chem. Phys. Lett. **164**, 210 (1989).

[14] A. Aizman and D. A. Case, Electronic structure calculations on active site models for 4-Fe,4-S iron-sulfur proteins, J. Am. Chem. Soc. **104**, 3269 (1982).

[15] D.-T. Chen *et al.*, Using hyper-optimized tensor networks and first-principles electronic structure to simulate experimental properties of the giant {*Mn*84} torus, arXiv preprint arXiv:2201.11979 (2022).

[16] A. Chiesa, F. Tacchino, M. Grossi, P. Santini, I. Tavernelli, D. Gerace, and S. Carretta, Quantum hardware simulating four-dimensional inelastic neutron scattering, Nat. Phys. **15**, 455 (2019).
[17] A. Kandala, A. Mezzacapo, K. Temme, M. Takita, M. Brink, J. M. Chow, and J. M. Gambetta, Hardware-efficient variational quantum eigensolver for small molecules and quantum magnets, Nature **549**, 242 (2017).
[18] G. Moula, T. Matsumoto, M. E. Miehlich, K. Meyer, and K. Tatsumi, Synthesis of an All-Ferric Cuboidal Iron–Sulfur Cluster [FeIII4S4 (SAr) 4], Angew. Chem. Int. Ed. **57**, 11594 (2018).
[19] A. Banerjee *et al.*, Proximate Kitaev quantum spin liquid behaviour in a honeycomb magnet, Nat. Mater. **15**, 733 (2016).
[20] P. Maksimov and A. Chernyshev, Rethinking $\alpha-RuCl_3$, Phys. Rev. Res. **2**, 033011 (2020).
[21] T. Suzuki and S.-i. Suga, Effective model with strong Kitaev interactions for $\alpha-RuCl_3$, Phys. Rev. B **97**, 134424 (2018).
[22] T. Suzuki and S.-i. Suga, Erratum: Effective model with strong Kitaev interactions for $\alpha-RuCl_3$ [Phys. Rev. B **97**, 134424 (2018)] Phys. Rev. B **99**, 249902 (2019).
[23] M. Gohlke, R. Verresen, R. Moessner, and F. Pollmann, Dynamics of the Kitaev-Heisenberg Model, Phys. Rev. Lett. **119**, 157203 (2017).
[24] P. Laurell and S. Okamoto, Dynamical and thermal magnetic properties of the Kitaev spin liquid candidate α-$RuCl_3$, npj Quantum Mater. **5**, 1 (2020).
[25] F. Arute *et al.*, Observation of separated dynamics of charge and spin in the Fermi-Hubbard model, arXiv preprint arXiv:2010.07965 (2020).
[26] C. Neill *et al.*, Accurately computing the electronic properties of a quantum ring, Nature **594**, 508 (2021).
[27] A. M. Souza, G. A. Álvarez, and D. Suter, Robust Dynamical Decoupling for Quantum Computing and Quantum Memory, Phys. Rev. Lett. **106**, 240501 (2011).
[28] J. Zhang, A. M. Souza, F. D. Brandao, and D. Suter, Protected Quantum Computing: Interleaving Gate Operations with Dynamical Decoupling Sequences, Phys. Rev. Lett. **112**, 050502 (2014).
[29] S. Widmann, V. Tsurkan, D. A. Prishchenko, V. G. Mazurenko, A. A. Tsirlin, and A. Loidl, Thermodynamic evidence of fractionalized excitations in $\alpha-RuCl_3$, Phys. Rev. B **99**, 094415 (2019).
[30] J. Nasu, M. Udagawa, and Y. Motome, Vaporization of Kitaev Spin Liquids, Phys. Rev. Lett. **113**, 197205 (2014).
[31] J. Nasu, M. Udagawa, and Y. Motome, Thermal fractionalization of quantum spins in a Kitaev model: Temperature-linear specific heat and coherent transport of Majorana fermions, Phys. Rev. B **92**, 115122 (2015).
[32] Quantum Computer Datasheet, http://quantumai.google/hardware/datasheet/weber.pdf
[33] https://github.com/hczhai/FeS-Heisenberg-DMRG-Data
[34] H. Zhai and G. K.-L. Chan, J. Chem. Phys. **154**, 224116 (2021).